Trinity College Dublin
Coláiste na Tríonóide, Baile Átha Cliath
The University of Dublin

4B7 Computer Aided Design

Optimisation of a UAV Drone Frame for Wildfire Detection

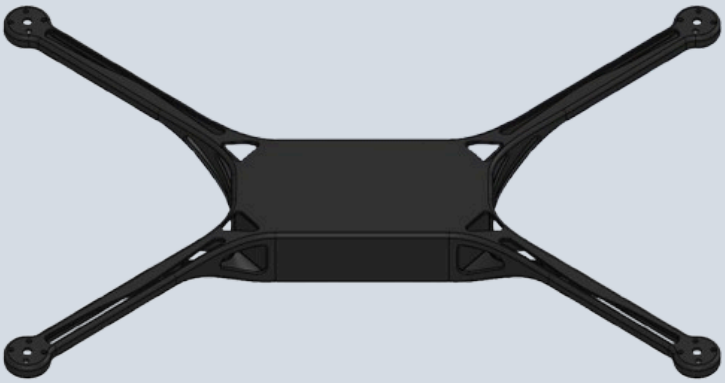

Group 4:

Finn O'Connor 22336740
Magnus Runham 22336288
Michael Sadlier 22336873
Peter Hamilton 22337384
Robert Dillon 22336720

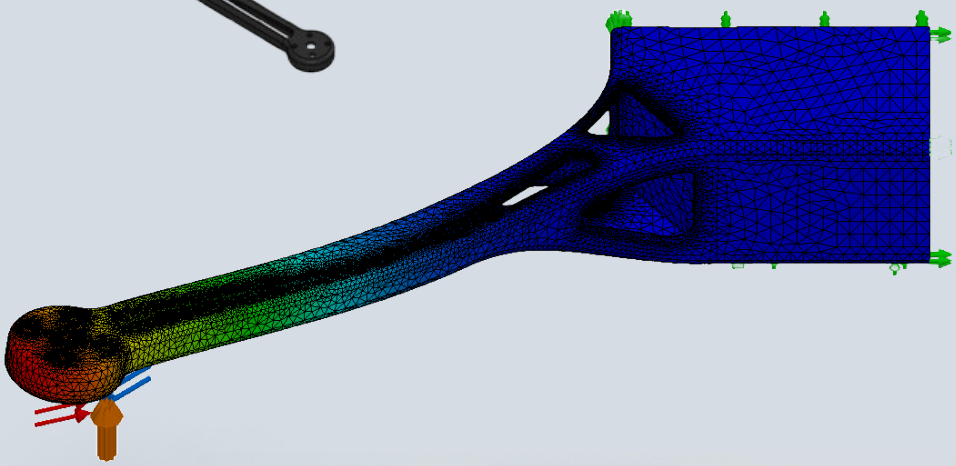

Contents

1 Final Design

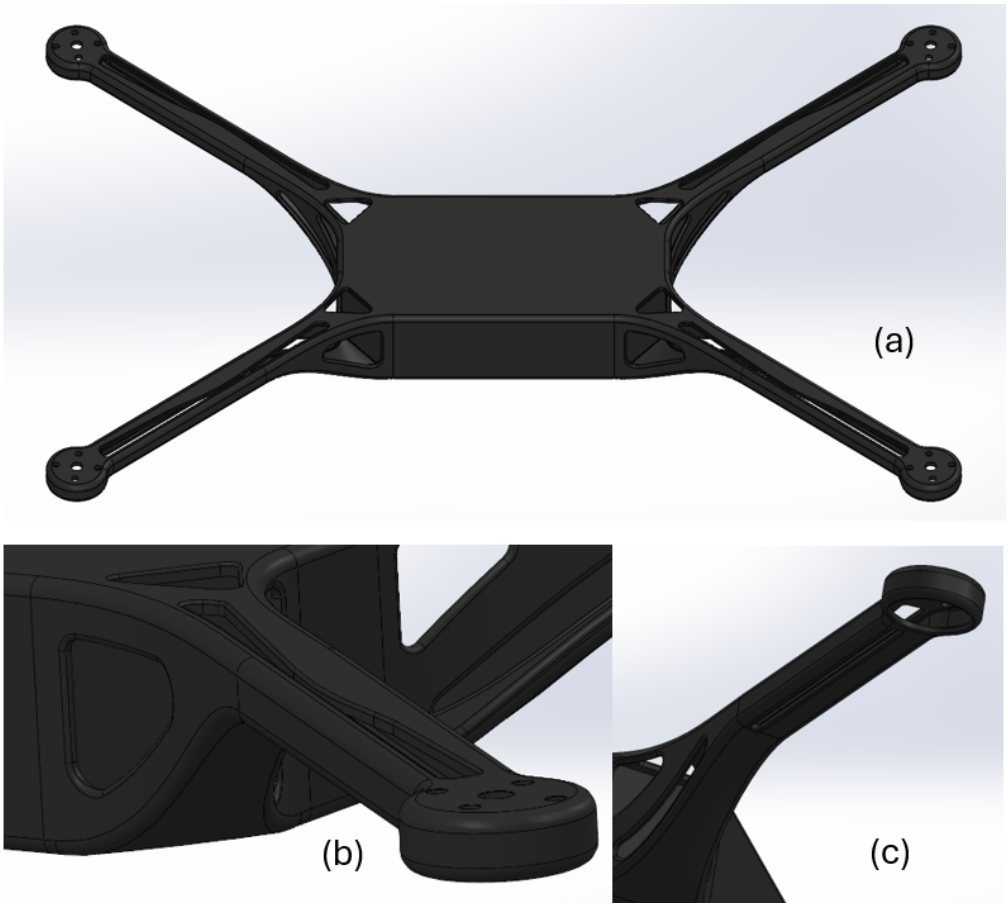

Figure 1: Full UAV frame design (a). Close-up of the arm from the top (b). Close-up of the arm from the bottom (c).

Figure 1 shows our final UAV design. The design reflects a refined and structurally efficient solution developed through iterative redesign, topology-informed cut-outs, and mesh-verified FEA analysis. The frame uses a shelled internal structure with a 2 mm wall thickness. This reduces mass while keeping the primary load paths the same. The UAV was manufactured in black anodised 7075-T6 aluminium. The design benefits from the alloy's high mechanical performance. The aluminium alloy has a yield strength above 500 MPa, elastic modulus of $\sim$ 72 GPa, and displays good thermal conductivity. The anodised finish provides improved surface durability and slightly enhanced thermal emissivity, which supports heat dissipation around high-load motors. It was also chosen for aesthetic purposes.

In worst-case thrust and torque loads, the final frame recorded a maximum von Mises stress of only $\sim$ 11 MPa. This gives the frame a strength ratio of approximately 2 % relative to the alloy's yield strength. This indicates a large safety margin against structural failure. The maximum displacement of 0.248 mm confirms a high level of bending stiffness. This is reflected in the design's overall stiffness of 1247 N/mm and a specific stiffness of approximately 3.0 (N/mm)/g for the 7075-T6 final frame. Thermal resistance also remained low at 4.3 K/W, meaning the frame can effectively conduct heat away from the propulsion system. With a mass of 420 g, the final geometry offers an excellent strength-to-weight balance and superior rigidity while maintaining manufacturability. Overall, the final design is lightweight, stiff, and strong. This meets performance requirements for UAVs operating in high-temperature or harsh weather conditions.

2 Problem Statement

Unmanned Aerial Vehicles (UAVs) are increasingly being used for everyday tasks. With over 900,000 drones registered in the United States [1]. UAVs such as drones are now used in industries such as farming, filming, and service industries. The drone industry is rapidly expanding, with estimates that it will reach over €90 billion by 2030 [2]. This is largely driven by companies' needs for faster and more efficient ways to move product and services.

One of the intended applications for UAVs is for wildfire monitoring and mapping. In these conditions it is vital that they can operate in extreme and unpredictable thermal environments. Wildfires in the United States have rapidly grown in intensity and frequency. There are approximately 60,000 wildfires annually in the United States [3], with around 7 million acres of land being destroyed [4]. During wildfires, ambient temperatures in affected zones can reach 40 °C–50 °C, while radiant heat from fire fronts can exceed several hundred degrees.

These hostile environments reveal the limitations of several current UAVs. They are commonly too heavy, lack the required strength or stiffness, and demonstrate poor thermal dissipation. Poor thermal properties can prevent motors and electronics from expelling heat effectively during sustained high-power flight. These issues reduce flight time, stability, and reliability. Such problems are critical when UAVs are relied upon for fire mapping crew decisions.

Wildfire seasons in many regions are now three times longer than they were in the 1970s [5]. There is now increasing pressure on UAV manufacturers to design vehicles that are lightweight, stiff, strong, and capable of efficient thermal regulation. Making these adjustments could fill a gap in the UAV market and meet the demands of wildfire response operations.

2.1 Initial Model

The initial UAV model was defined using a 5 propeller, $L = 140\,\text{mm}$, $W = 80\,\text{mm}$, and $\theta_1 = \theta_2 = 45°$, following the geometric layout in Figure 2. The central hub was sized to provide sufficient space to house all required internal components. A full list of component dimensions and masses is provided in Appendix A.

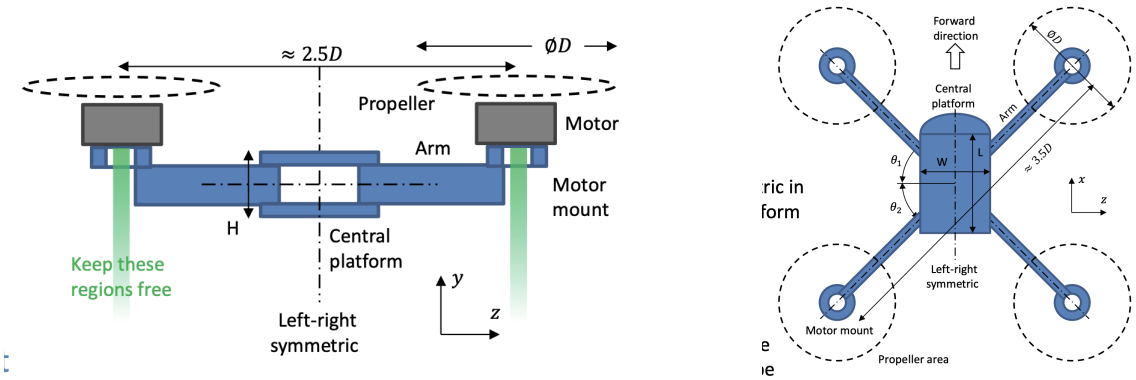

(a) Side view of quadcopter layout.

(b) Top view of quadcopter layout.

Figure 2: Quadcopter geometry schematics [6].

3 Design Process

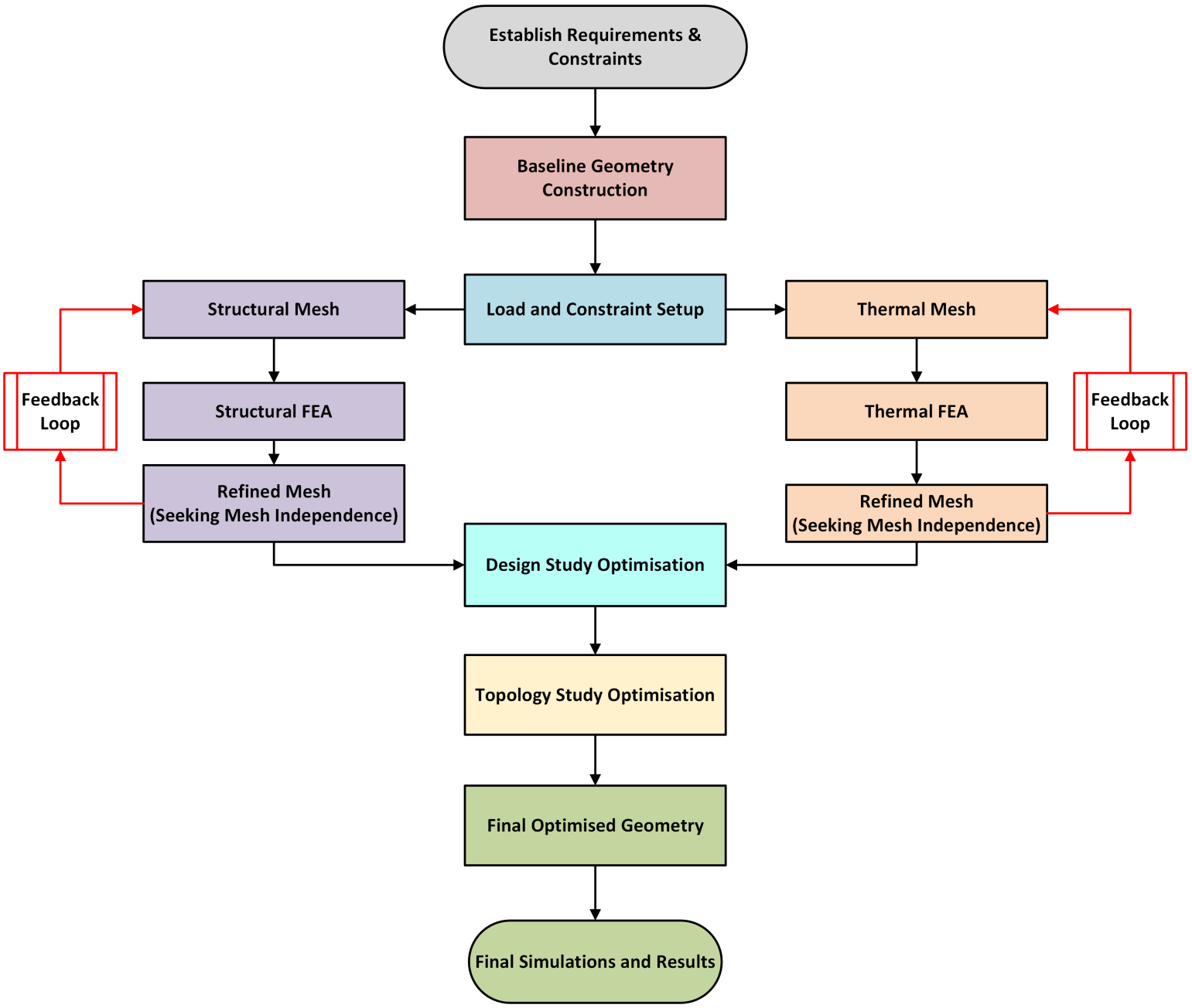

Figure 3: Flow chart explaining our design process.

- **Establish Requirements and Constraints**
- **Baseline Geometry Construction**
- **Load and Constraint Setup**
- **Structural Mesh Refinement**
- **Thermal Mesh Refinement**
- **Design Study Optimisation**
- **Topology Study Optimisation**
- **Final Geometry, Simulations, and Results**

4 Mesh Refinement Study

4.1 Overview

All mesh-independence studies were performed on a simplified UAV model representing the basic model provided in the brief. The simplified frame model used a loft feature to create rounded geometry along with fillets. This way of modelling ensured that no unrealistic stresses built up along sharp edges and corners, and excluded arm cut-outs and motor-mount details to ensure that mesh-independence results were independent of geometric complexity.

For the mesh-independence studies, a generic linear-elastic material was applied (6061-T4). This allowed isolation of numerical mesh effects without introducing variations due to material properties. Final material selection was performed later in the design study. Two mesh refinements were carried out for the structural and thermal study.

4.2 Boundary Conditions and Loading

This section describes the fixtures, structural loads, and thermal loads applied to the simplified UAV arm model for each mesh-independence study. The UAV was modelled using symmetry about the two orthogonal planes, allowing for a quarter of the model to be analysed without altering the physical response.

For the structural case, the UAV arm was constrained using symmetry and a roller–slider fixture at the root. An upward load was applied at the upper surface of the motor mount to represent the thrust force. To capture the torsional effects generated by the motor, two additional loads were applied: a moment acting along the arm's longitudinal axis and a torque applied around the motor-mount support, as illustrated in Figure 4. The specific base loading values can be found in Table 5.

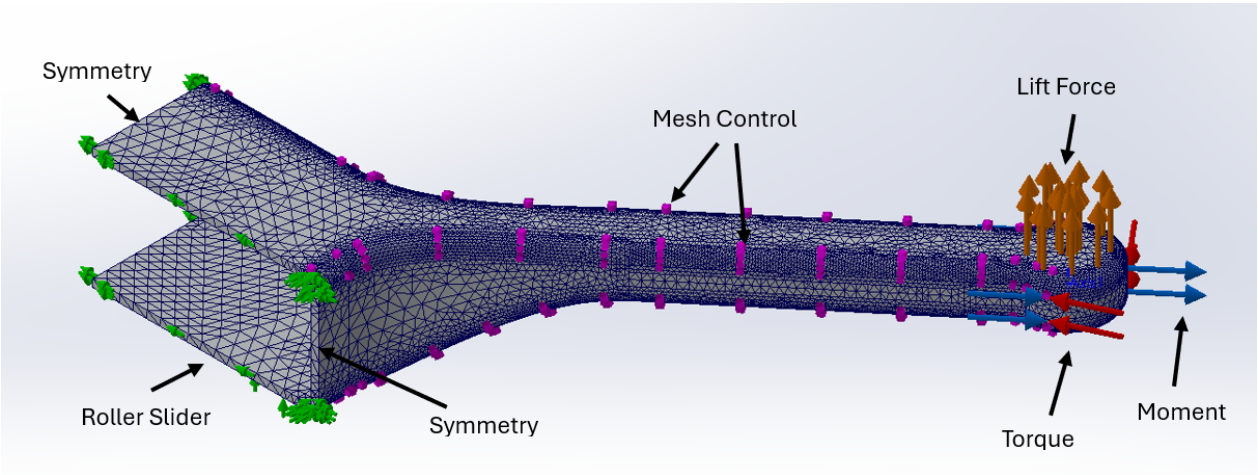

Figure 4: Boundary conditions and applied loads for the UAV arm model.

For the thermal analysis, a heat load was applied to the motor region to represent the power dissipated as waste heat. Following the design brief, the motor was assumed to convert 2 % of its electrical input power into heat under level-flight conditions. Unlike the structural case, the thermal loads were based solely on level-flight operation, as transient fluctuations in heat generation were assumed to average out over time. The other exposed surfaces of the arm had a natural convection boundary condition of $h = 40\,\mathrm{W/(m^2\,K)}$ and a temperature of 300 K (27 °C) as stated in the brief. These conditions capture the steady-state thermal behaviour of the UAV arm during realistic flight conditions. For mesh refinement, a 2.63 W thermal load was used.

4.3 Structural Mesh

The global mesh was refined using a global element size of 4 mm, while the mesh control was refined incrementally from 4 mm–0.5 mm (Table 1) adn can be seen in the graphs in Figure 5. The maximum displacement converged immediately, suggesting that the bending stiffness is unaffected by further refinement. Similarly, the equivalent strain energy values extracted from the `.out` file remained unchanged across all meshes, confirming that the overall deformation behaviour is fully mesh independent.

Table 1: Data from manual stepwise mesh control refinement using constant global element size (4 mm).

Manual stepwise mesh refinement	**Global mesh element size**	**Number of elements N_e**	**Max displacement (mm)**		**Max stress (MPa)**		**Equivalent strain energy (J)**	
			Value	**Rel. error**	**Value**	**Rel. error**	**Value**	**Rel. error**
Too coarse	4	19,744	0.044	N/A	3.6750	N/A	4.135E-04	N/A
Coarse	2	33,486	0.044	0.00%	3.7110	0.97%	4.135E-04	0.00%
Standard	1	109,242	0.044	0.00%	3.7060	0.13%	4.135E-04	0.00%
Fine	0.5	423,601	0.044	0.00%	3.7020	0.11%	4.135E-04	0.00%

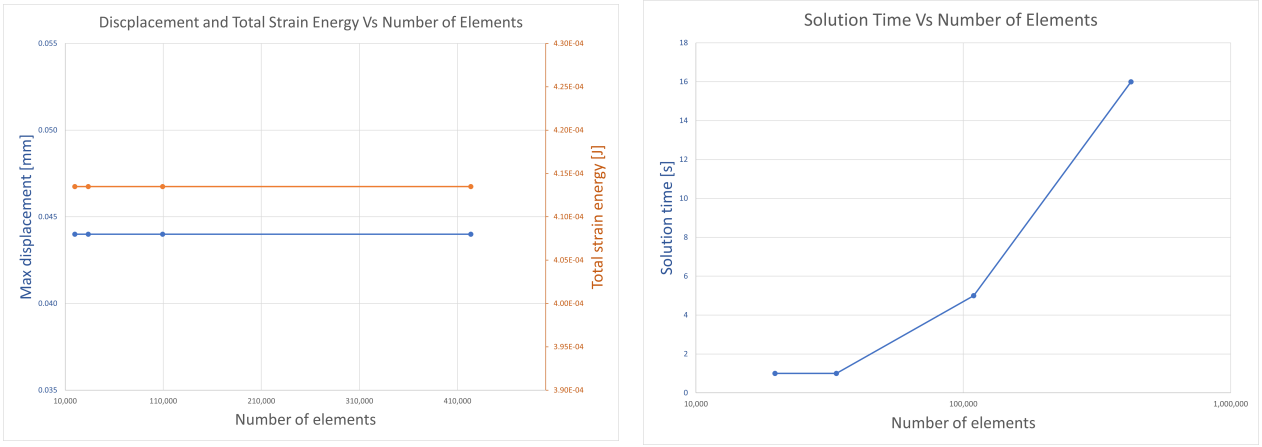

(a) (b)

Figure 5: Mesh convergence plot (a) showing that displacement and TSE convergence as mesh is refined. Computational time vs number of elements (b) showing the increase in computational power as the number of elements increase.

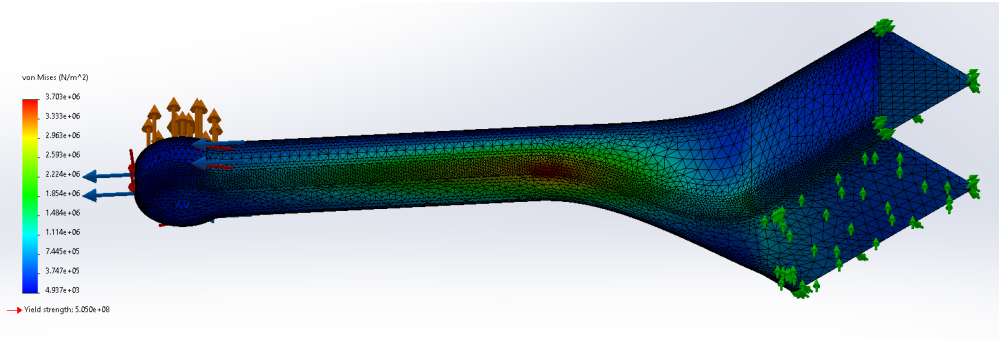

Figure 6: Structural mesh of the UAV arm.

The maximum stress showed minor variations between the coarse and standard meshes, with the relative error decreasing from 0.97 % to 0.13 %, and refinement to 0.5 mm produced only a negligible change of 0.11 %. This shows that the mesh stabilises once the mesh size reaches approximately 1 mm, with no meaningful improvement from additional refinement. Based on these results, the standard mesh was selected as it provided the necessary balance between computational efficiency and numerical accuracy for the structural case.

4.4 Thermal Mesh

The thermal mesh refinement study was performed on the baseline UAV design using a manual stepwise approach, reducing the global element size from 8 mm to 1 mm to determine the convergence of the predicted maximum temperature. A thermal power load of 2.64 W was applied to represent the heat generated during operation, and a natural convection boundary condition of 40 W/(m^2 K) was applied to all external faces, using the same method as described in Section 7. As shown in Table 2, refining the mesh increased the element count, rising from 17,211 to 679,932 elements for the 1 mm mesh. However, the predicted maximum temperature remained constant at 33.85 °C across all refinement levels, with a relative error of 0.00 %. This behaviour indicates that the thermal solution is mesh independent and that temperature gradients within the arm are sufficiently smooth to be captured even by relatively coarse meshes.

Table 2: Thermal mesh refinement data.

Manual Stepwise Mesh Refinement	**Global mesh element size**	**Number of elements N_e**	**Max temperature**	
			Value	**Rel. error**
Too Coarse	8	17,211	33.85°C	N/A
Coarse	4	30,489	33.85°C	0.00%
Standard	2	113,575	33.85°C	0.00%
Fine	1	679,932	33.85°C	0.00%

As a result, the standard mesh element size of 2 mm was selected for the optimised UAV's thermal analysis studies, due to the fact that further refinement did not yield any improvement in accuracy but substantially increased the computational load.

5 Design & Topology Studies

5.1 Design Study

The basic UAV arm model, using the 1 mm mesh from Section 4, was used in a parametric design study to optimise the cross-sectional geometry. The objective was to minimise mass while maintaining stiffness and strength; the strength ratio $(\sigma_{vM,\max}/\sigma_y)$ was kept comfortably below unity and stiffness was assessed via $k = F/\delta$. Worst-case loading was applied as a distributed thrust at the mounting flange with a torsional moment about the mount, and the maximum allowable deflection was limited to 1% of $1.75d$ to ensure no deflection.

Two geometric parameters, the arm width $b \in [8\,\mathrm{mm}, 16\,\mathrm{mm}]$ and arm height $h \in [10\,\mathrm{mm}, 20\,\mathrm{mm}]$, were tested. Tests that exceeded any constraints (the stress limit or the deflection limit) were discarded and the remaining feasible set of dimensions were ranked by mass and specific stiffness.

Table 3: Summary of design study variables, constraints, and goals.

Category	**Parameter**	**Description**
Variables	Arm Width (mm)	Varied between 8 mm and 16 mm.
	Arm Height (mm)	Varied between 10 mm and 20 mm.
Constraints	Max. Stress (σ_{max})	$\leq$ 0.5 of yield strength.
	Max displacement	1% of 1.75 d
Goals	Mass	**Minimise**

The selected dimensions were $b = 12\,\mathrm{mm}$ and $h = 18\,\mathrm{mm}$. This configuration satisfied the stress and deflection limits with a favourable stiffness-to-mass balance and clean manufacturability. The final arm was drafted with gentle fillets, the specified motor-mount interface and hole pattern, and consistent wall thickness for printability. A close-up of the motor-mount region and the final section is shown in Figure xx.

5.2 Material Selection

The frame for UAVs that are used for wildfire-monitoring must display:

- High strength-to-weight ratio
- High tensile strength
- High toughness
- Good thermal performance

Although carbon fibre is a common material in UAVs, it was not modelled as it is a composite and anisotropic. Aluminium alloys 6061-T6 and 7075-T6 were analysed instead, as they are isotropic, easily machinable, suitable for SolidWorks FEA, and widely used in UAV frames. These alloys offer a balance of low density, high stiffness, good tensile strength, and excellent thermal conductivity.

Table 4: Mechanical and thermal properties of aluminium alloys 6061-T6 and 7075-T6 [7, 8, 9].

Property	**6061-T6**	**7075-T6**
Density (kg/m^3)	2700	2810
Young's Modulus (GPa)	68.9	72
Tensile Strength (MPa)	310	580
Yield Strength (MPa)	276	500
Thermal Conductivity (W/m·K)	167	140
Melting Range (°C)	617	505

Aluminium 7075-T6 is significantly stronger and slightly stiffer, making it a better candidate for minimising deflection under thrust and manoeuvre loads. Aluminium 6061-T6 provides superior thermal conductivity and excellent manufacturability, making it suitable for components requiring efficient heat dissipation. All of these characteristics are required for wildfire-monitoring UAVs operating under higher temperatures and demanding mechanical loading.

For the final UAV frame, aluminium 7075-T6 was chosen as it provides the highest strength and stiffness of the considered alloys. This ensures minimal deformation under thrust, torque, and manoeuvre loading. This makes it the most reliable option for wildfire-monitoring missions where structural rigidity is critical.

5.3 Topology Study

A topology study was carried out to derive the most material-efficient structural layout for the UAV arm and the central hub while satisfying the stiffness, mass, and manufacturability constraints. This stage formed the foundation for the final design geometry. It also was a critical step in ensuring the structural and thermal analysis could be carried out.

Optimisation Setup

The topology study used the results from the design study and tried to optimise them. The one quarter of the frame generated by the design study was used in the study to reduce the computational cost. Unlike the design study, the topology study did not use symmetry. This also reduced the computational demand. The body was fixed using fixed geometry on the bottom surface in place of symmetry. The structural loads were taken from the propulsion and loading calculations. The motor thrust, reaction torque, and inertial loads were applied to the motor-mount interface. The opposite end of the arm was constrained using fixed geometry. This loading strategy reflects a real flight condition where the arm must transfer the torque and thrust generated by the motor and propeller to the body without excessive displacement.

The optimisation was performed by using a static compliance minimisation objective, equivalent to maximising the stiffness for a given mass. A volume fraction constraint was applied, which typically retained 20–30% of the design space material depending on the run. This ensured that a lightweight structure was generated.

Design Space and Constraint

The design space consisted of the full arm volume between the motor mount and the hub connection. Non-design regions were defined for features that must remain fully solid, such as the motor-mount plate, bolt locations, and the central interface geometry. Manufacturing constraints were included to ensure the output was feasible for additive manufacturing or CNC machining.

Optimisation Procedure

A series of runs were carried out with progressively refined resolution. The initial run used a coarse voxel density to identify the general load paths. Subsequent runs increased the resolution to capture finer features and stabilise the geometry. Each iteration balanced stiffness and manufacturability, until a valid design emerged.

Throughout the optimisation process, displacement and stress constraints were monitored to ensure that the resulting designs remained below allowable deflection limits and within the material's yield strength range. Due to the nature of topology optimisation being iterative, several cycles of adjusting constraints, re-running the optimisation, and interpreting the resulting geometry were required before coming to a final conclusion. The design insight plot shown in Figure 7 gave us a sense of where the maximum loads occurred in the UAV arm, enabling us to verify if the results yielded in the topology study were valid.

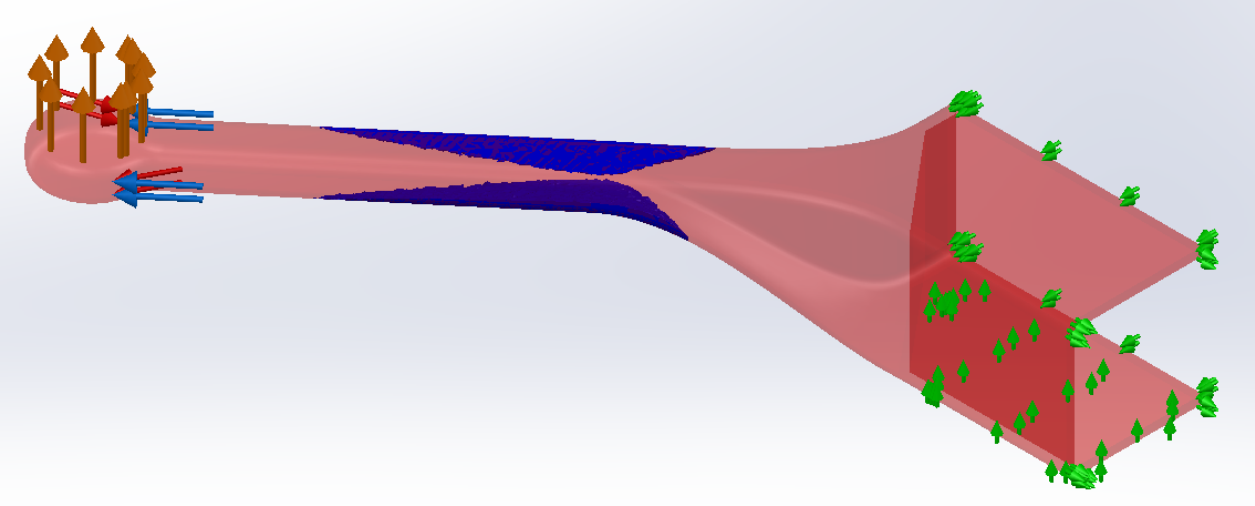

Figure 7: Design insight plot showing the regions under maximum load (blue).

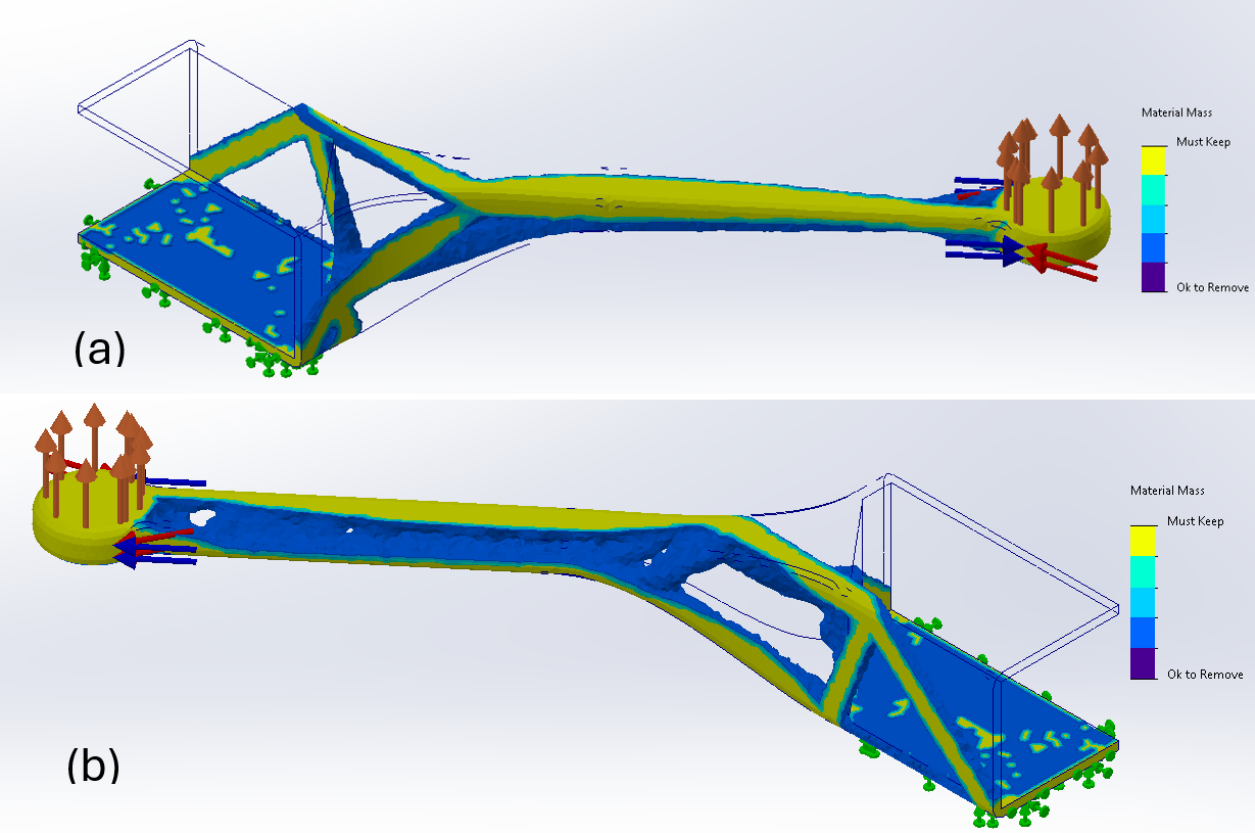

Figure 8: Results of the topology study indicating the regions that mass could be removed (purple/blue) and the mass that must be kept (yellow).

Topology Optimisation Results

The topology result highlighted a clear load path in yellow from the motor mount into the central hub via a pair of struts. The blue/purple regions identified the mass that could be removed. This formed the basis for the final CAD geometry.

The optimised density field was exported and used as a template for a parametric solid model. Using a

shell model with a thickness of 2 mm, the structure was hollowed out according to the optimised topology. Extruded cuts were then used to cut away excess material that was not needed. Features were cleaned, filleted, and thickened to ensure that the structure retained its performance capabilities. Non-design regions, such as the bolt holes and mount, were merged with the optimised topology to form a finished design.

The final design resulted in a quarter-structure that had a mass of 105 g. Compared to the initial geometry, which had a mass of 263.75 g, there was an overall mass decrease of 60.2 %. This was achieved without compromising the design's structural integrity. The final design can be seen in the

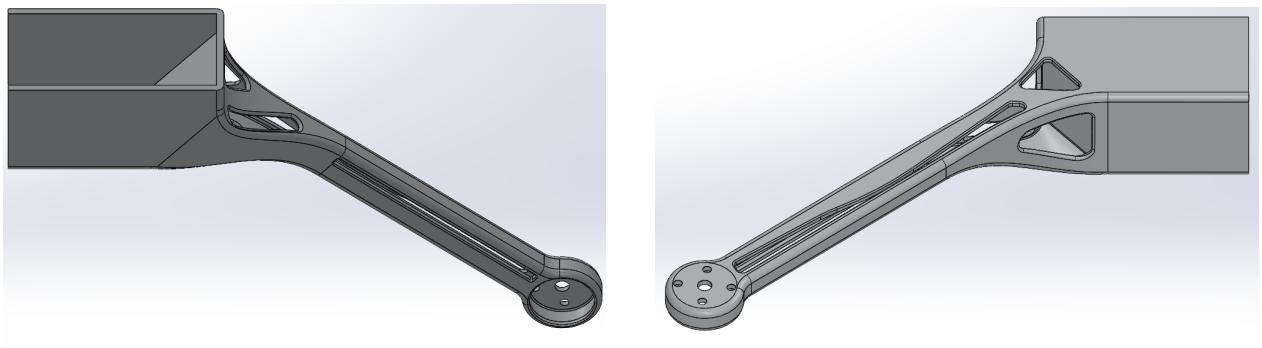

(a) (b)

Figure 9: Final design showing views from (a) the top plane and (b) the bottom plane.

6 Structural Analysis

The structural analysis was conducted using the values in Table 5. The formulas used to calculate these values can be found in Appendix A. A 4 mm global mesh element size with a 2 mm control mesh element size was used.

Table 5: Structural load inputs for UAV frame analysis.

Structural load parameter	**Baseline value**	**Optimal value**
Total mass (frame + components)	1838 g	1202.5 g
Mass per motor + propeller	33 g	33 g
Hover thrust per motor ($L_{\min}$)	4.58 N	2.95 N
Structural load factor (G)	4	4
Required thrust per motor ($L_{\max}$)	16.73 N	10.50 N
Motor torque (nominal)	0.090 Nm	0.059 Nm
Motor torque (worst case)	0.3605 Nm	0.24 Nm

The structural analysis was performed on a simplified final model, with the shell but without the cut-outs, as the cut-outs introduced solver instabilities. The results can be deemed as an accurate representation of how the final model would perform, as it was identified in the topology study and design insight study that there were no critical load paths in those regions of material.

Stress Results and Strength Ratio

The maximum von Mises stress from the simplified model was

$$\sigma_{\text{vm,max}} = 11.08\,\text{MPa},$$

identified on the underside of the arm near the motor mount, as shown in Figure 10.

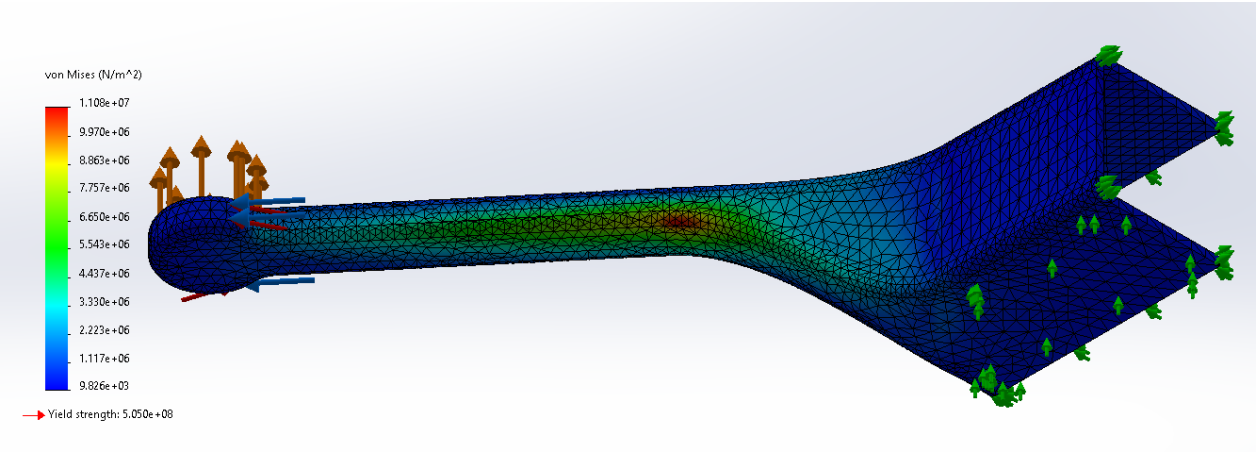

Figure 10: Von Mises stress distribution for the simplified UAV frame under worst-case loading.

The strength ratio is defined as the ratio of maximum von Mises stress to the yield strength of the material:

$$\text{Strength ratio} = \frac{\sigma_{\text{vm,max}}}{\sigma_y} \times 100\,\%.$$

Using a yield strength of $\sigma_y = 505\,\text{MPa}$ for 7075-T6 aluminium gives

$$\text{Strength ratio} = \frac{11.08}{505} \times 100\,\% \approx 2.19\,\% \approx 2.2\,\%.$$

Thus, the frame operates at only about $2.2\,\%$ of the yield strength under the worst-case loading, providing a very large safety margin against yielding.

Displacement, Stiffness and Specific Stiffness

The displacement simulation was run using the full final design (including cut-outs) to capture the true stiffness of the optimised frame. The maximum resultant displacement was $\delta_{\text{max}} = 0.2479\,\text{mm}$, occurring at the tip of the arm, as illustrated in Figure 11.

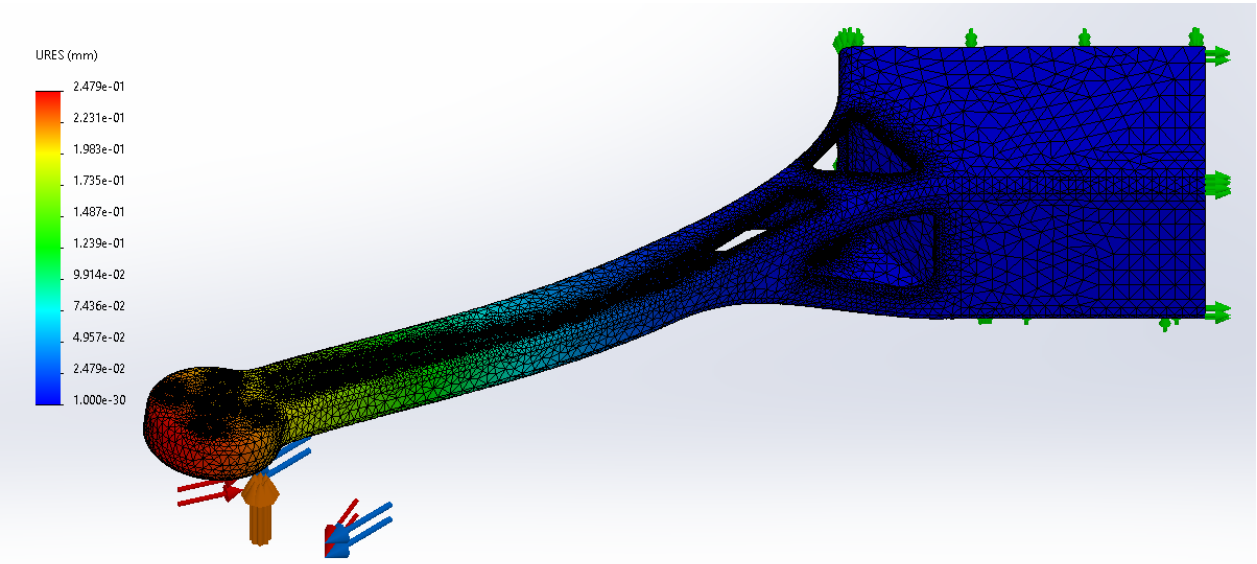

Figure 11: Resultant displacement plot for the final UAV frame design under worst-case loading.

The global flexural stiffness k of the arm is defined as

$$k = \frac{F}{\delta_{\max}},$$

where F is the applied equivalent load at the motor. For the applied load used in the simulation, this gives

$$k \approx 1247\,\mathrm{N/mm}.$$

The mass of the quarter-frame of the final design is $m_{1/4} = 105\,\mathrm{g}$. The specific stiffness is therefore

$$k_{\text{spec}} = \frac{k}{m_{1/4}} = \frac{1247}{105} \approx 11.9\,(\mathrm{N/mm})/\mathrm{g}.$$

This high specific stiffness shows that the final frame is both lightweight and rigid, which is essential for maintaining propeller alignment and overall flight stability under high load factors.

7 Thermal Analysis

The thermal analysis tests were carried out on the optimised UAV design using a global standard mesh element size of 2 mm. A heat load was applied to the motor region to represent the power dissipated as waste heat. In line with the design brief [6], the motor was assumed to convert 2 % of its electrical input power into heat under level-flight conditions, resulting in a thermal load of 1.48 W per motor. This heat was applied as a uniform Heat Power load across the mounting flange, the same face to which the lifting force was applied in Figure 4, to replicate the transfer interface of contact between the motor and the UAV. Similarly, all external surfaces of the UAV frame were assigned a natural convection boundary condition with a heat transfer coefficient of 40 W/(m^2 K), as specified in the brief, to replicate heat loss to the surrounding air during flight. The ambient temperature was set to 300 K, with an emissivity of 0.05 for unfinished aluminium. No fixtures were required, as this was a static thermal study.

For a 300 K ambient temperature, the maximum temperature of the UAV reached 36.7 °C, and the minimum was 27 °C, indicating that heat was not evenly distributed. There is a noticeable 2.85 °C difference between identical heat loads in our baseline and optimised designs, but this was deemed a worthwhile trade-off to reduce the UAV's mass by approximately 35 %, as shown in Table 5. The maximum temperature of 36.7 °C is well within the operating range of the chosen material, aluminium 7075-T6, which has a melting point of around 505 °C as seen in Table 4.

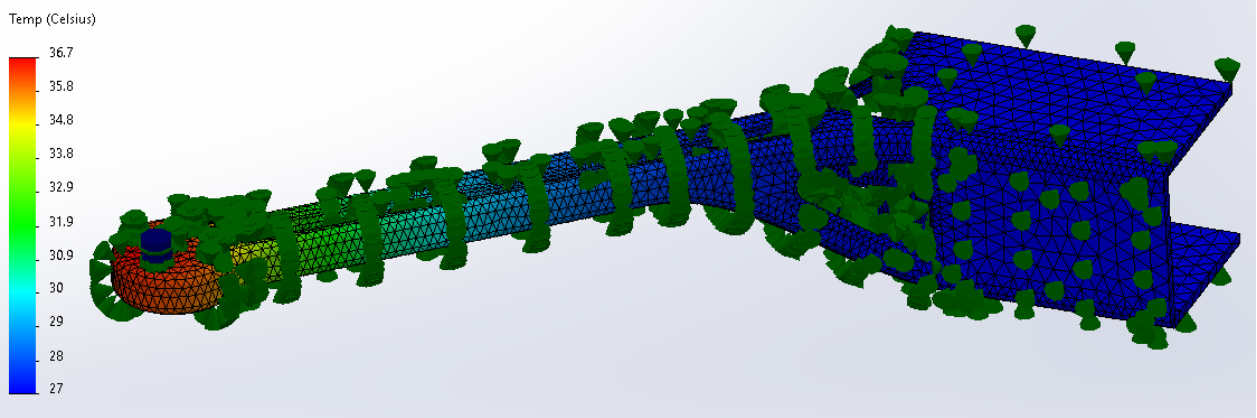

Figure 12: Temperature plot using a 2 mm global mesh and 300 K ambient temperature.

A similar thermal test was carried out at 350 K to simulate harsher operating conditions and assess the UAV's suitability for wildfire monitoring and mapping, where it will be subject to higher ambient temperatures and effective heat dissipation is critical for the UAVs' safety and endurance.

For a 350 K ambient temperature, the UAV's maximum temperature reached 86.7 °C, and the minimum was 77 °C, as shown in Figure 13. This indicates uneven heat distribution with hot spots around the motor region, but notably has the temperature range of 9.7 °C as the 300 K test, suggesting similar spatial gradients under both conditions. Benchmarked against material limits, these temperatures remain comfortably within safe operating margins for aluminium 7075–T6, which has a melting temperature of about 505 °C (Table 4).

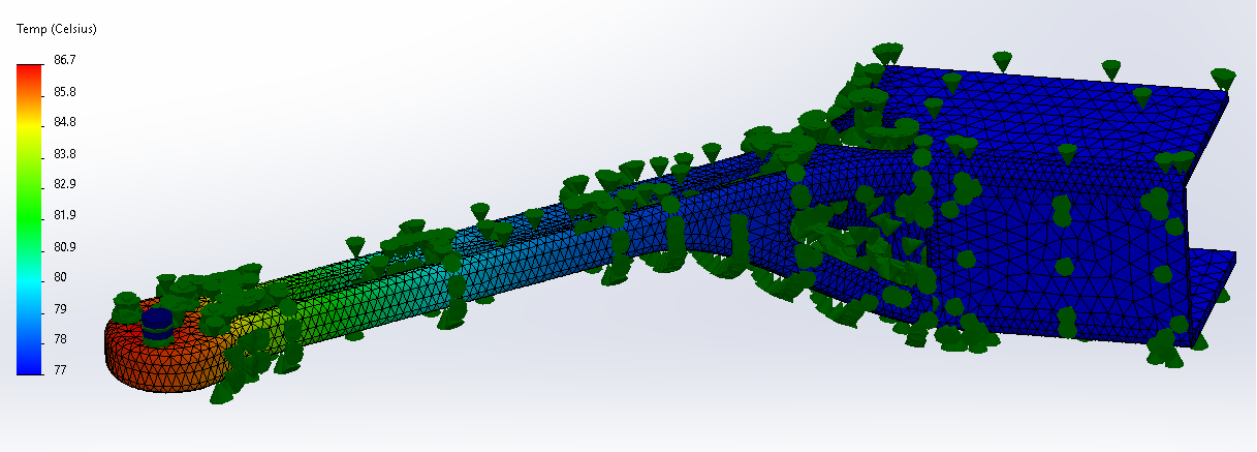

Figure 13: Temperature plot using a 2 mm global mesh and 350 K ambient temperature.

A final thermal simulation was run at 350 K with a simulated anodised aluminium finish (emissivity 0.9). Radiation was modelled in SolidWorks and applied to the same external surfaces as the convection boundary conditions. The effect was minimal: the maximum temperature was 86.1 °C, a negligible change from the previous 350 K case of 86.7 °C, and it remains well below the melting point of aluminium 7075-T6. The maximum temperature remains far below the melting point of aluminium 7075-T6; however, it may cause heat damage to internal components. In order to execute a full assessment of transient heating across all components, it would require a time-dependent thermal study, which was beyond the scope of this static analysis.

8 Summary

The final UAV frame meets structural and thermal performance targets. Under bending and torsion, it shows very low displacement (around 0.25 mm) and stresses around 11 MPa, well below the 7075-T6 yield strength, indicating high stiffness and a wide safety margin. Thermal studies at 300 K and 350 K reached maxima of 36.7 °C and 86.7 °C, respectively, with 86.1 °C for the anodised finish case, all comfortably below material limits. Based on these conditions, the UAV frame would be suited for use in wildfire detection.

A Structural and Thermal Load Calculations

Table 6: Central hub component specification and mass breakdown.

Component	Qty	Dimensions (mm)	Volume (mm^3)	Unit mass (g)	Total mass (g)
Pixhawk 2.4.8 flight controller	1	$82 \times 50 \times 16$	65600	73	73
M8N GPS module	1	D50 $\times$ 14	700	32	32
ESC BLHeli 30A	4	$50 \times 30 \times 15$	22500	28	112
Power distribution board	1	$46 \times 36 \times 4$	6624	9	9
Camera	1	$28 \times 28 \times 20$	15680	38	38
RFD 868X telemetry kit	1	$57 \times 30 \times 13$	22230	15	15
Flysky FS-iA6B receiver	1	$47 \times 26 \times 15$	18330	15	15
LiPo battery 6S 1050mAh	1	$76 \times 40 \times 37$	–	200	200
Internal Hub Components Total			151664	—	626

A.1 Structural Load Definitions

Minimum lift for level flight (1G)

$$4L_{\min} = mg, \qquad L_{\min} = \frac{mg}{4}$$

Internal arm load (1G)

$$F_{\min} = L_{\min} - m_1 g$$

Motor torque at hover

$$T_{\min} = 0.02\, L_{\min}$$

Worst–case thrust (4G manoeuvre)

$$L = G\, L_{\min}$$

Worst–case internal force

$$F = G\, F_{\min}$$

Worst–case motor torque

$$T = G\, T_{\min}$$

Bending moment at arm root

$$M_{\text{bend}} = F\, \ell_{\text{arm}}$$

Multiplier

$$G = 4$$

A.2 Thermal Load Definitions

Electrical input power

$$P = VI$$

Motor heat dissipation (2% of electrical power)

$$q = 0.02\, P$$

Convection boundary condition

$$h = 40\,\mathrm{W/(m^2\,K)}, \qquad T_\infty = 300\,\mathrm{K}$$

References

[1] F. A. Administration, "U.s. drone registration statistics 2024," 2024, available at: https://www.faa.gov (Accessed 2024).

[2] M. Intelligence, “Drone market - growth, trends, forecasts (2024–2030),” 2024, forecast estimating the global drone market to exceed €90 billion by 2030.

[3] U. F. Service, “National report on wildfire activity,” 2023, reports over 60,000 U.S. wildfires annually.

[4] N. I. F. Center, “Wildland fire summary and statistics annual report,” 2022, documents wildfire acreage exceeding 7 million acres in severe years.

[5] N. E. Observatory, “Wildfire seasons increasing in length globally,” 2020, indicates wildfire seasons are three times longer compared to the 1970s.

[6] T. Persoons, “Assignment 3: Uav frame optimisation,” 2025.

[7] A. International, *ASM Handbook Volume 2: Properties and Selection: Nonferrous Alloys and Special-Purpose Materials*. ASM International, 1990.

[8] “Aluminum 6061-t6 material datasheet,” https://www.matweb.com/search/datasheet.aspx?matguid=0a4e8c9ca8d44b678b9b352e8cc7b6aa.

[9] “Aluminum 7075-t6 material datasheet,” https://www.matweb.com/search/datasheet.aspx?matguid=4eafbb8d7d9540a59b6e82ddf6e80811.